Comparison and Validation of Different Magnetic Force Microscopy Calibration Schemes

NANO MICRO
small

Small, DOI: 10.1002/smll.201906144

Comparison and Validation of Different Magnetic Force Microscopy Calibration Schemes

Héctor Corte-León, Volker Neu, Alessandra Manzin, Craig Barton, Yuanjun Tang, Manuela Gerken, Petr Klapetek, Hans Werner Schumacher, and Olga Kazakova*

Comparison and validation of different magnetic force microscopy calibration schemes

Héctor Corte-León, Volker Neu, Alessandra Manzin, Craig Barton, Yuanjun Tang, Manuela Gerken, Petr Klapetek, Hans Werner Schumacher, and Olga Kazakova.*

Dr. Héctor Corte-León,
National Physical Laboratory, Hampton Road, Teddington TW11 0LW, United Kingdom.
E-mail: hector.corte@npl.co.uk

Dr. Volker Neu,
Leibniz IFW Dresden, Helmholtzstr. 20, 01069 Dresden, Germany.

Dr. Alessandra Manzin,
Istituto Nazionale di Ricerca Metrologica, Torino, I-10135, Italy.

Dr. Craig Barton,
National Physical Laboratory, Hampton Road, Teddington TW11 0LW, United Kingdom.

Yuanjun Tang,
Leibniz IFW Dresden, Helmholtzstr. 20, 01069 Dresden, Germany.

Manuela Gerken,
Physikalisch-Technische Bundesanstalt, Braunschweig, D-38116, Germany.

Dr Petr Klapetek,
Department of Nanometrology, Czech Metrology Institute Okružní 31, 638 00 Brno, Czech Republic

Dr. Hans Werner Schumacher
Physikalisch-Technische Bundesanstalt, Braunschweig, D-38116, Germany.

Dr. Olga Kazakova
National Physical Laboratory, Hampton Road, Teddington TW11 0LW, United Kingdom.

Keywords: MFM, calibration, magnetic probes, Hall nano-sensors, nanoscale,

ABSTRACT

The future of consumer electronics depends on the capability to reliably fabricate nanostructures with given physical properties. Therefore, techniques to characterize materials and devices with nanoscale resolution are crucial. Among these is magnetic force microscopy, which transduces the magnetic force between the sample and a magnetic oscillating probe into a phase shift, enabling the locally resolved study of magnetic field patterns down to 10 nm. Here, it is shown the progress done towards making quantitative MFM a common tool in nano-

characterization laboratories. We demonstrate the reliability and ease-to use of the calibration method based on a magnetic reference sample, with calculable stray field, and a deconvolution algorithm. This is achieved by a comparison with other two calibration approaches, using numerical modelling as a quantitative link: measuring the probe's impact on the voltage signal when scanning above a nano-sized graphene Hall sensor; and recording the MFM phase shift signal when the probe scans across magnetic fields produced by metallic micro-coils. Furthermore, in the case of the deconvolution algorithm, it is shown how it can be applied using the open-source software package called Gwyddion. We also report the estimated magnetic dipole approximation for the most common probes currently in the market.

1. Introduction

Magnetic force microscopy (MFM) is a widely used well-established scanning probe microscopy-based (SPM) imaging technique in nanomagnetism research[1]. MFM transduces magnetic field gradient into images using an oscillating probe composed of a magnetic tip and a flexible cantilever that reveals a frequency shift in reaction to the magnetic tip-sample coupling.

Nowadays, as other SPM imaging modes, e.g. electrostatic imaging, MFM usually comes as a default feature in commercial SPMs, however, despite its extensive implementation, it remains a qualitative tool in most of the laboratories where it is being used. The difficulty to convert the data obtained with MFM into quantitative values is mainly due to two sources of uncertainty[2], namely the tip-sample interaction affecting each other's magnetization, and the lack of knowledge of tip's stray field. To overcome the first source of uncertainty, researchers usually take images of samples varying the measurement parameters and conditions[1]. For instance, typical ways of detecting artefacts in the imaging process include: changing scan direction; varying scan size; modifying imaging speed; increasing/decreasing distance to sample's surface; adding an externally applied magnetic field; or using probes with different

magnetic properties. By comparing the results, it is possible to come to an understanding of when there is a significant tip-sample interaction or when it can be considered negligible. The second source of uncertainty is nevertheless more difficult to tackle, as other magnetic field imaging techniques with nanoscale resolution, and capable of characterizing MFM probes, are also difficult to calibrate and hence introduce errors into the measured probe's stray field. For instance, electron imaging was used to investigate the stray field distribution arising from an MFM probe[3][4][5], and by comparing that to known sources of magnetic field (e.g. a known electrical current passing through a straight wire), it is possible to quantify the field amplitude. However, in general the results based on electron imaging are proportional to the integral of the magnetic and electric fields along the electron's path, and thus require complex calculations to retrieve the magnetic field at a specific location. A different approach consists in imaging nanostructured magnetic materials with known coercive field. By performing hysteresis loop measurements with the tip close to the surface, it is possible to estimate the additional field contribution from the tip on the switching event[6][7]. However, the magnetic field produced by an MFM probe is highly non-uniform, while the coercive field of the nanostructured material is generally measured in a uniform field, hence when biasing the sample with the probe's field the measurement only provides a rough estimation of the field produced by the probe[8]. Alternatively, the opposite approach to characterize the probe's stray field consists in modifying the MFM probes by replacing the magnetic material with nanostructures of easier to model magnetization, e.g. magnetic nanoparticles, and thus inferring the probe's stray field by means of numerical modelling[9][7]. However, although replacing the tip with another nanostructure simplifies the problem of extracting the probe's stray field, accurate measurements of the magnetic properties of the nano-sized object are required, and thus another technique capable of measuring magnetic field with nanoscale resolution is still needed.

Other two approaches also use nanostructures, the first one employs a nano-sized Hall cross to measure the stray field from the tip[10], while the other uses nanopatterned coils to generate known magnetic fields and then estimates the tip's field from the resulting image[11][12]. Nevertheless, none of these calibration techniques has been fully implemented as a standard operation procedure. The main difficulty is that they required either special probes and additional equipment to the scanning probe microscope or significant numerical calculations to reconstruct the tip-sample interaction.

A very successful procedure, first introduced by Hug et al. in 1998[13] and now regularly applied in several National Metrology Institutes[14][2], uses the concept of tip transfer function (TTF), and relies only on a thin film of known magnetic properties (i.e. reference sample). The advantage of the TTF approach resides in the few steps needed to calibrate MFM probes, and the ease to obtain quantitative field values once probes have been calibrated. This approach uses a reference sample with calculable stray field and a deconvolution of the measured and calculated stray fields to derive the TTF. An implementation of this deconvolution algorithm including suitable filters to take into account instrumental noise is available in the open-source SPM software package Gwyddion[15]. Once the TTF is determined, further MFM measurements taken with the calibrated probe can be converted into quantitative field data again by a deconvolution procedure (which is also implemented in the Gwyddion package).

Here, we demonstrate the validity and ease of use of the TTF approach by calibrating several MFM probes and, based on their TTF, confirming the quantitative results obtained from other two alternative calibration methods: (i) the one based on passing current through micron-size coils to create a known magnetic field and subsequent MFM characterization; (ii) the one based on measuring the tip's stray magnetic field using graphene nano-size Hall crosses. The results shown demonstrate that the TTF approach, in combination with the used reference sample, successfully estimates the z-component (i.e. out-of-sample's plane) of the probe's

tip's stray field for a range of commercial MFM probes. This is shown by comparing the experimental measurements on the graphene nano-sized Hall crosses with numerical simulations based on the probe's stray field estimated by the use of the TTF. With the aid of the micron-size coils, the results additionally demonstrate that the reference sample used in the TTF approach defines the probe's interacting volume during the calibration measurement (i.e. the volume of magnetic material in the probe that contributes to the obtaining of the final MFM image), and that the interacting volume at the same time determines which features can be quantified when performing MFM imaging[12]. This is demonstrated by showing that any dipole approximation that matches the TTF can reproduce the results obtained with the used graphene Hall cross, while in the case of the coils only a specific dipole expansion of the TTF fits the experimental results. Additionally, it is shown step-by-step how to use the software package Gwyddion to analyze measurements from reference samples to obtain the TTF. Thus, the overall conclusion is that the probe's stray field estimation obtained through the TTF approach can be easily and reliably used to reproduce the tip-sample interaction when the *z*-component dominates, and when the volume of the magnetic probe interacting with the sample's stray field is similar to the one probed by the used reference sample.

2. Results

In order to demonstrate the ease to use of TTF and its reliability, three different calibration techniques were employed (see the Experimental Section for details on fabrication of samples). These techniques are based on: a reference sample composed of Co/Pt multilayers; a sample with a 200 nm sized graphene Hall cross; and a sample with an embedded 2 µm sized Au coil. Due to the different nature of the samples and the quantities being measured, standard 2-pass MFM imaging had to be modified to take into account the particularities of each sample.

2.1. Tailored imaging modes

Figure 1 summarizes the three imaging modes used with the three types of samples used. The first mode (Figure 1(a)) is the **standard 2-pass MFM** mode, which was used for the Co/Pt sample. In this mode the MFM probe oscillates close to its resonance frequency, f_0, while it scans over the sample's surface. Both probe and sample are grounded. During the first pass (Figure 1(a) Pass I), the feedback loop keeps the amplitude at a constant value fixed by the setpoint, while the *Z*-piezo moves the probe up and down to track the surface. During the second pass (Figure 1(a) Pass II), the *Z*-piezo reproduces the topography measured during the first pass adding a constant height h_{lift}. The imaging then tracks the phase shift, $\Delta\varphi$, between the harmonic oscillatory excitation of the probe and the harmonic oscillation of the cantilever. Common difficulties of this mode are the selection of a value of h_{lift} too small for which there is still a significant contribution of the topography to the phase signal, or electrostatic interaction that can compete with the magnetic interaction in the final image definition. In the results presented here, the first difficulty was minimized by ramping the distance *Z* while monitoring the oscillation amplitude, to select the best setpoint for the first pass and a lift height large enough, so the probe has entered the free oscillation regime[16]. In the case of the Co/Pt sample, the total distance used during the second pass was 100 nm or 150 nm (some of the probes require a higher distance to be used also with the rest of the samples). By having a conductive sample, as it is the case for the Co/Pt, and a conductive probe, as it is the case for the commercial probes tested here, both grounded, the second criticality was also minimized. The second mode, **phase modulated-MFM-Kelvin-probe force microscopy** (PM-MFM-KPFM), was adopted to image the micron-size embedded coils. When imaging the embedded micro-coils electrostatic interaction became a major issue due to the insulating layer used for the embedding together with the amplitude of the electrical current passing through the coil and required to generate the magnetic field, thus electrostatic compensation (i.e. Kelvin-probe force microscopy) was needed[10]. In this mode, the probe also oscillates close to its resonant

frequency f_0. During the first pass (Figure 1(b) Pass I), the feedback loops keeps the amplitude constant and the *Z*-piezo traces the surface while the probe scans. To compensate the effect of the electrostatic field the Kelvin-probe force microscopy uses an AC voltage to probe interaction and then applies a voltage V_{DC} to the probe to null it (see Ref[10] for further details of how the Kelvin-probe feedback loop operates). During the second pass (Figure 1(b) Pass II), the *Z*-piezo reproduces the topography measured during the first pass adding a constant height h_{lift}. Now, no AC excitation voltage is applied to the probe, instead the voltage $V_{DC,}$ measured during the first pass, is applied again to the probe to compensate the electrostatic interaction. As in standard MFM, the image is obtained tracking the phase shift, $\Delta\varphi$, between the harmonic oscillatory excitation of the probe and the harmonic oscillation of the cantilever. It is important to note that while performing Kelvin-probe measurements during the second pass would in principle result in better compensation (because electrostatic force will decay with distance and thus the force will not be the same during the first pass and the second one). However, the electrostatic contribution at elevated height is more susceptible to cross-talk with the magnetostatic contribution, such that the chosen two-pass method is preferred.

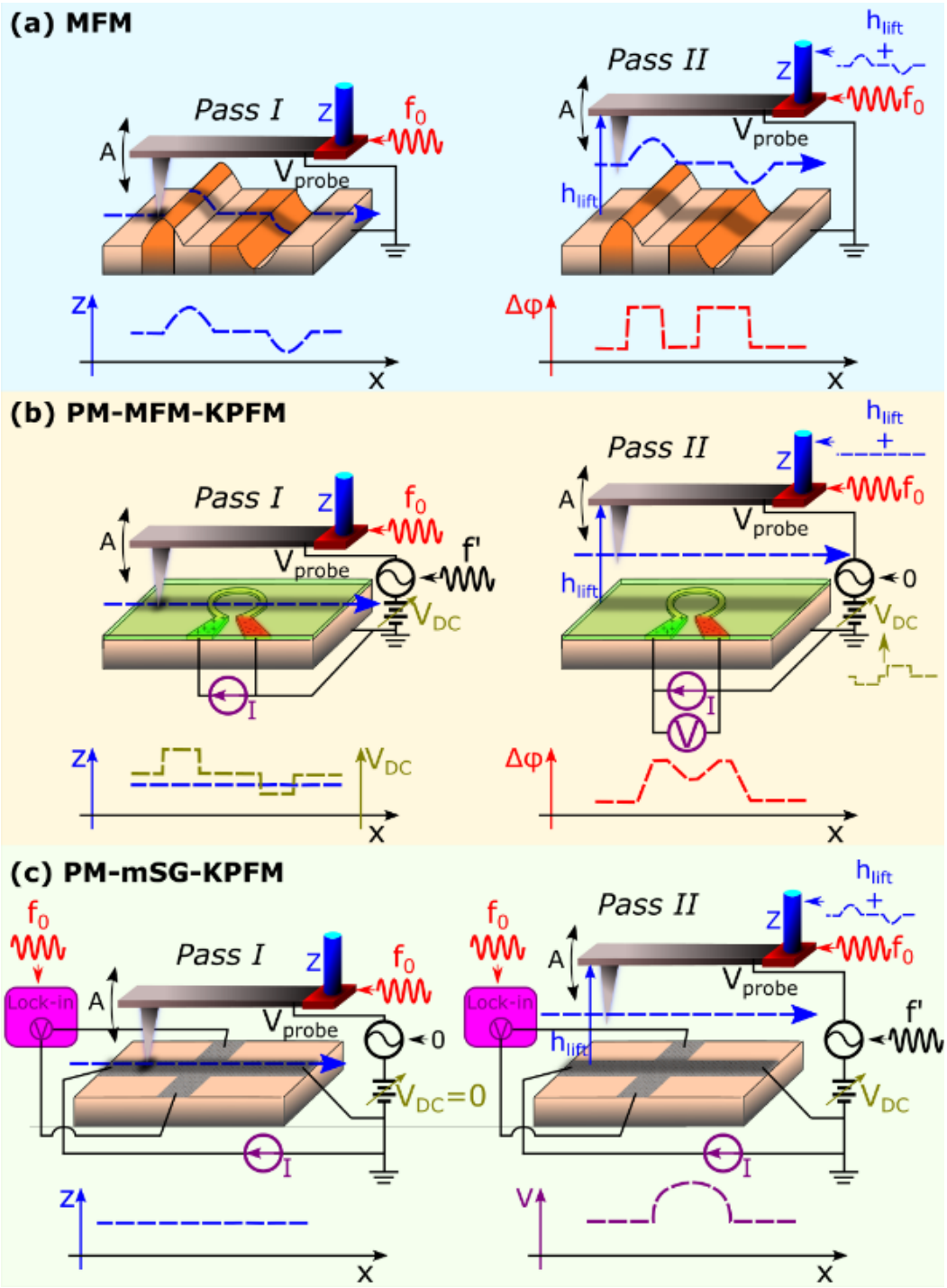

Figure 1. Schematics of the imaging methods used. (a) MFM. (b) PM-MFM-KPFM. (c) PM-mSG-KPFM.

The last mode used, **phase modulated-magnetic scanning gate-Kelvin-probe force microscopy** (PM-mSG-KPFM) was employed to scan the nano-sized graphene Hall cross. The mode is also a 2-pass mode where the first pass is used to track the topography and the second pass is used to measure the response of the Hall sensor to the probe's stray field.

During the first pass the probe is oscillated close to its resonance frequency f_0 and the feedback loop moves the *Z*-piezo up and down to keep the amplitude constant and thus track the surface (Figure 1(c) Pass I). During the second pass (Figure 1(c) Pass II), the *Z*-piezo reproduces the topography adding a constant lift height, h_{lift}, and an AC voltage is applied to the probe to detect the electrostatic interaction, which is then canceled by applying a DC voltage V_{DC}. Simultaneously, a constant current is passed through the Hall sensor and a lock-in amplifier is used to measure perpendicularly to the current. The lock-in is synchronized with the probe's oscillation, thus picking up only the signal that corresponds to the presence and oscillation of the probe and omitting the overall magnetic background generated by the close proximity between the Hall sensor and the magnetic probe. In this case, contrary to the previous mode, there is no cross-talk between electrical and magnetic signals, and thus the Kelvin-probe compensation can be done during the second pass without the risk of adding any undesired effects to the signal. Moreover, due to the extreme sensitivity of graphene to electrical fields, a good electrical compensation was needed in order to be able to detect the signal corresponding only to the magnetic interaction.

2.2. Probes used

Table 1 summarizes the mechanical properties of the commercial probes used during the experiments. These probes were selected from different manufacturers, having a good response to at least one of the three imaging modes described before, and for spanning a range of different magnetic moments owing to the thickness, or material, of the magnetic coating. In this study, we use the commercial names of the probes as provided by the manufacturers.

Table 1. Mechanical properties of the probes used. Colors indicate the same manufacturer. The manufacturer's name is given in italics and the probe's commercial name is given in bold.

Probe	Resonance frequency [kHz] [a)]	Quality factor [a)]	Spring constant [N/m] [a)]
PPP-MFMR *Nanosensors*	71.9 ±0.2	185 ±12	5.7 ±1.4
PPP-MFMR *Nanosensors* #2	70.68 ±0.04	195 ±4	4.4 ±0.2

PPP-LM-MFMR *Nanosensors*	74.0 ±0.2	184 ±9	4.4 ±0.2
HR-MFM75 ML1 *TeamNanotec*	81.46 ±0.06	219 ±12	7.8 ±0.5
MESP V2 *Bruker*	75.0 ±0.2	192 ±21	8.3 ±2
MESP V2 *Bruker #2*	80.8 ±0.02	216 ±7	6.5 ±0.2
MESP HM V2 *Bruker #2*	82.5 ±0.04	276.8 ±8	8.0 ±0.2
MESP LM V2 *Bruker*	72.7 ±0.04	204.9 ±5	3.6 ±0.2
MFM01 *TipsNano*	60.53 ±0.04	182 ±5	4.489 ±0.2
MFM_LM *TipsNano*	80.44 ±0.02	217 ±3	6.1 ±0.2
MFM_LM *TipsNano #2*	60.53 ±0.04	182.17 ±3	4.5 ±0.2

[a)] ± standard deviation based on three measurements.

For further details on probe's characteristics, including frequency spectrum and SEM images with main dimensions, see Supporting Information.

2.3. Calibration process

In order to compare the TTF calibration with the other two calibration techniques, an imaging protocol (shown in **Figure 2**), was designed and followed for each of the probes described in Table 1. It consists in imaging the Co/Pt sample and measuring the spring constant and Q factor in between imaging the other two samples (i.e. graphene Hall cross and micron-size coil), while keeping the scan parameters the same (i.e. distance to sample, oscillation amplitude, pixel size). From the MFM images of the Co/Pt film, using the TTF deconvolution algorithm (see the Experimental Section for further details), the gradient of the probe's stray field was extracted. Then, the field gradient, approximated by a dipole, was used in the numerical modelling to simulate the result of imaging the graphene Hall cross or the micron-sized coils. At this point, different values of the spring constant, the quality factor or the dipole approximation were used to identify damage in the probes. Finally, the protocol ends by comparing the results of the numerical model with the experimental results.

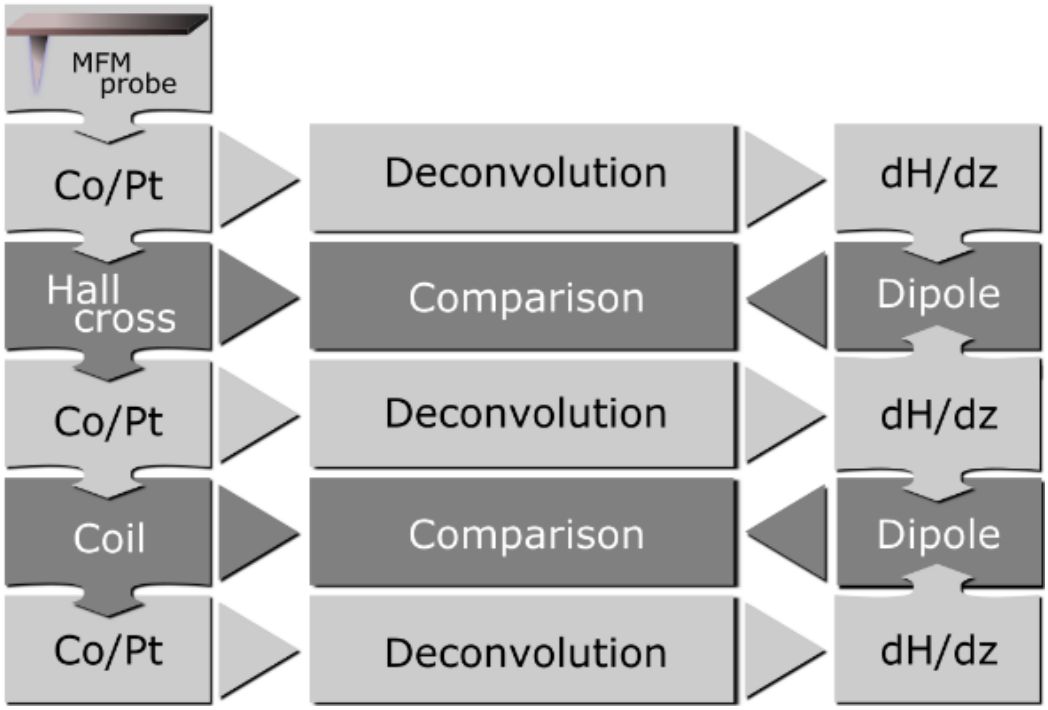

Figure 2. Calibration process. For each probe the sequence of measurements consists in imaging the Co/Pt film in between imaging the Hall cross and the coil. The images from the Co/Pt were then deconvolved to obtain the probe's magnetic field gradient (i.e. $\frac{dH}{dz}$), and subsequently, the dipole approximation. Numerical modeling, using the dipole approximations, were then compared with the experimental data from the use of the Hall cross and the coil.

Figure 3 shows the resulting images of the Co/Pt film, Hall device, and coil, measured with the PPP-MFMR Nanosensors probe following the protocol described in Figure 2 (see the Experimental Section for further details). Figure 3(a) shows topographical and magnetic images of Co/Pt (topography in the first pass in (1) and two repetitions of the magnetic phase, i.e. the second pass, in (2) and (3)). The reference Co/Pt film, as it can be seen, breaks into meander domains with perpendicular magnetization. Clear edges between domains indicate that the distance to the sample during the second pass was appropriate. A repetition of the second pass imaging has been done to identify artefacts and to reduce the effect of random noise. As it was mentioned in the protocol (see Figure 2), probe degradation is one of the main issues affecting quality of scanning, hence, to control the process of probe degradation,

the TTF calibration step (i.e. imaging the CoPt) was repeated again (see Figure 3(c) and (d)) in between imaging of the other two samples.

The next step corresponds to the imaging of the graphene Hall cross (Figure 3(b)). Topography of the sample is shown in (1), whereas surface potential and the amplitude of the Hall signal are shown in (2) and in (3), respectively. A good agreement between the trace and retrace surface potential scans, and an absence of dark and bright lobes at the corners of the Hall cross[17][10] are both clear indicators of a good electrostatic compensation.

After repeating the imaging of Co/Pt (i.e. Figure 3(c)), the coil was imaged (see Figure 3(d)). Topography is shown in (1), surface potential in (2), and the phase signal during the second pass in (3). As expected, the most intense signal in the phase image comes from the edges and interior of the coil. The last step of the protocol is repeating the Co/Pt measurement (Figure 3(e)) to obtain a final TTF calibration.

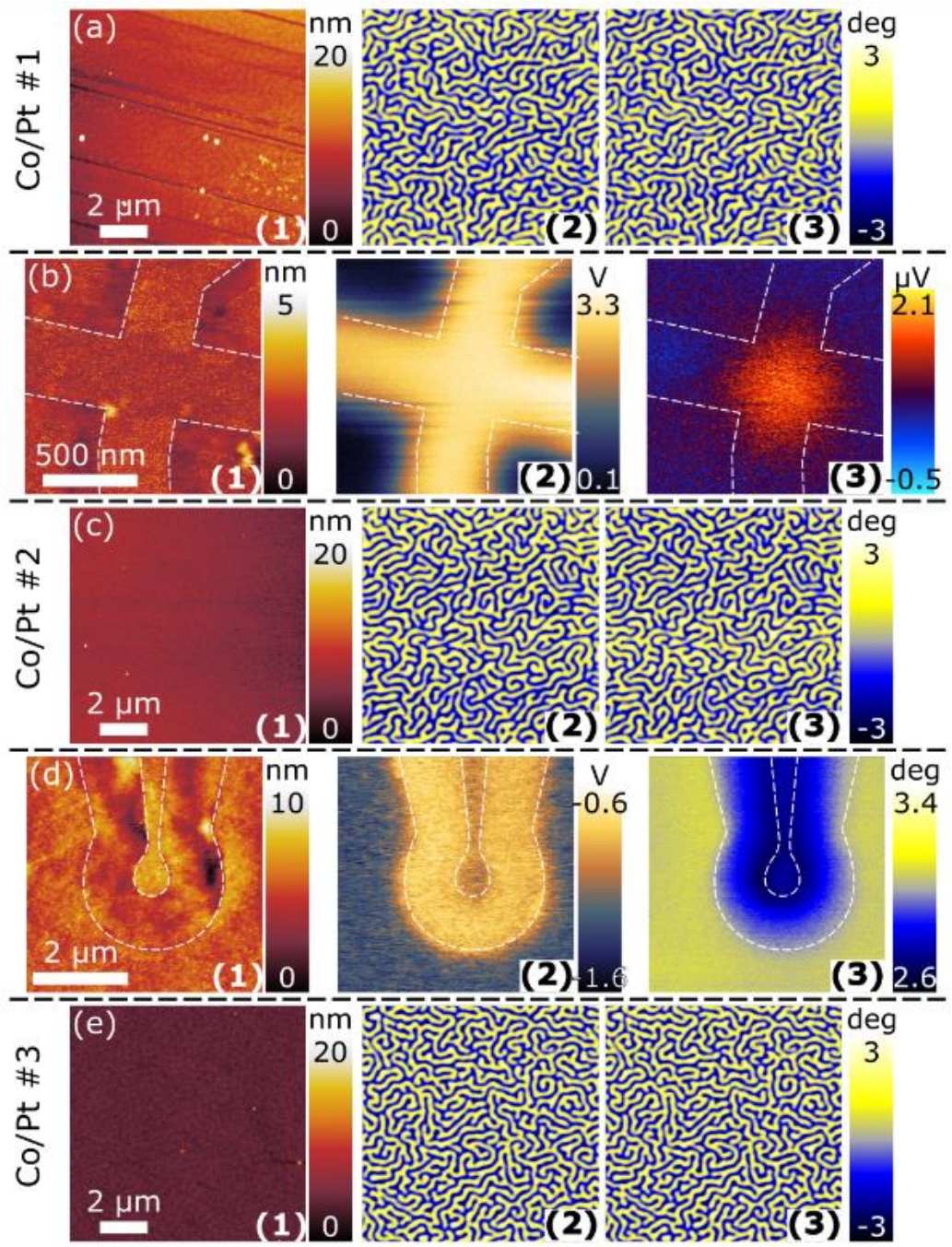

Figure 3. Sequence of measurements for a PPP-MFMR Nanosensors probe. (a) MFM on a Co/Pt sample: topography (1); phase during the second pass (2); and phase during the second pass on the second repetition of measurement (3). (b) FM-KPFM/mSGM on a graphene Hall cross: topography (1); V_{CPD} during the second pass (2); and electrical voltage measured across the sensor (3). (c) MFM on a Co/Pt as in (a). (d) FM-KPFM/MFM on a micro-coil: topography (1); V_{CPD} during the first pass (2); and phase during the second pass (3). (e) MFM on a Co/Pt as in (a) and (c).

After repeating the process described for the PPP-MFMR Nanosensors probe with all the probes listed in Table 1, the images of the Co/Pt samples were used to calculate the TTF and estimate the magnetic dipole approximation of the probe. TTFs were obtained from each

Co/Pt reference measurement by constructing an effective surface charge map, which takes into account the observed domain configuration and the magnetic properties of the sample. Deconvolving the measured image and the surface charge map with the help of a Wiener invert filter leads to the stray field derivative profile $\frac{\partial H_z^{probe}}{\partial z}(x, y)$ of the probe, which is named TTF in Fourier space. This process is described in **Figure 4** for the PPP-MFMR Nanosensors probe and in the images shown in Figure 3, for further details and a detailed theoretical background, see Experimental Section.

The dipole approximation, schematically shown in Figure 4(a), consists in approximating the probe's stray field gradient by the gradient produced by a magnetic dipole. To obtain this approximation, the TTF approach starts by converting the phase change images (e.g. Figure 3(e)(2)) into pixel area force gradient (Figure 4(b)), considering the spring constant and quality factor of the probe (see the Experimental Section). Then the up/down domains are differentiated to create a mask to simulate the stray field of the sample (shown as a red overlay in Figure 4(c)). Using the material parameters and the mask, the surface charge of the sample is calculated (Figure 4(d)). The pixel area force gradient and the surface charge (i.e. Figure 4(b) and (d), respectively) are then deconvolved to obtain the TTF (i.e. the gradient of the probe's stray field at sample's surface (Figure 4(e)). See the Experimental Section for a detailed description of how to perform this whole process using Gwyddion software.

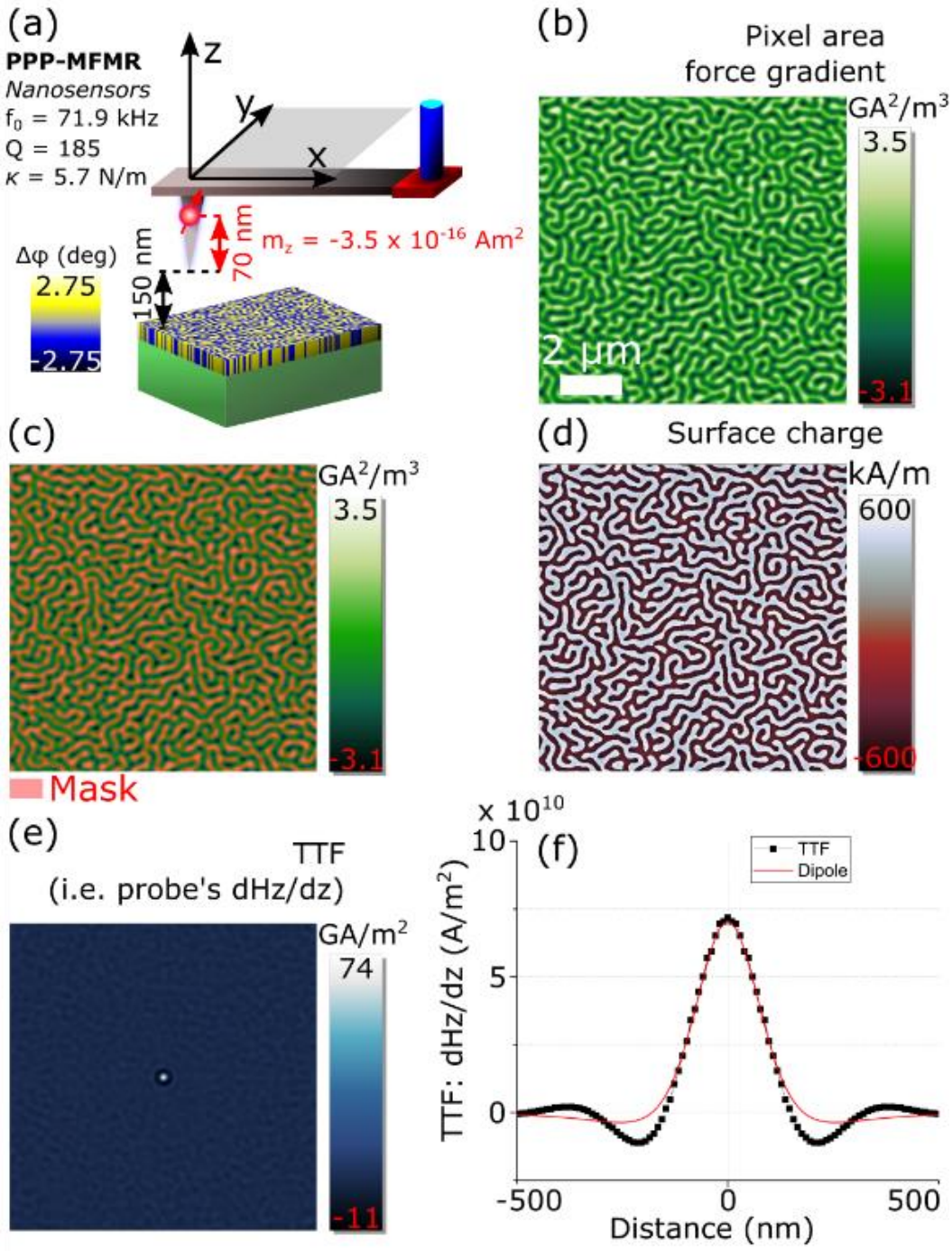

Figure 4. Process followed to approximate probe's stray field by a dipole for a PPP-MFMR Nanosensors probe. (a) Schematic of MFM on a Co/Pt sample indicating the distance to the sample during the second pass (i.e. 150 nm), the mechanical properties of the probe, and the value and position of the dipole (70 nm from probe's apex). (b) Conversion of phase shift image into pixel area force gradient using probe's mechanical properties. (c) Pixel area force gradient image masked to identify up/down domains in the Co/Pt sample. (d) Reconstruction of the sample's surface charge, using the mask from (c) and the material parameters. (e) TTF obtained using the surface charge shown in (d) and the pixel area force gradient in (b). (f) Circularly averaged profile of (e) alongside with the field gradient from a dipole located as in (a) and with the values indicated in (a).

In order to find the dipole that best reproduces the probe's stray field, when TTFs from the same probe agreed to within 10% (judged from the height of the central peak) they were averaged to reduce noise. For further noise reduction, the typical small asymmetry in the stray field profile due to the cantilever tilt has been neglected and the TTF matrices were circularly averaged around the central peak. The result for the PPP-MFMR Nanosensors is reported in Fig. 4f. Apart from the small errors introduced by the de-noising (Wiener filter) and the averaging processes, this real space TTF (RSTTF) is the correct quantification of the probe's imaging properties within the spatial frequency range provided by the reference sample and probed by the reference measurement (determined by image and pixel size). The best dipole fit is then found by calculating the field gradient created by the dipole and matching it with the profile extracted from the TTF. In the case shown here, for the PPP-MFMR Nanosensors probe the dipole has an amplitude of -3.45 × 10 -16 Am^2 and its located at a distance Z = 70 nm from the probe's apex. Using these values, the *z*-component of the field generated by the probe at 100 nm from the probe's apex is estimated in ~ 14 mT. It is important to notice that in order to fully reproduce the probe's field gradient a multipole expansion is required, however, as it can be seen in Figure 4(f), a dipole approximation is in general sufficient to capture most of the fields features.

Table 2 summarizes the results of the dipole approximation of all tips. It can be observed that in some cases the probes were stable through the whole process, and thus the dipole approximation is valid for all the Co/Pt measurements, while in other cases separate approximations have to be determined for each case. Note that probes classified as "high moment" have indeed higher values in the dipole approximation, while the ones classified as "low moment" tend to have lower values.

Table 2. Magnitude and position of the dipole for the approximation of the probe's stray field.

	Dipole		Probe's field at 100 nm from probe's apex.
Probe	m_z [Am^2]	Z [nm] from probe's apex.	B_z [mT]

PPP-MFMR *Nanosensors*			
Co/Pt #1, #2, and #3	-3.45 ×10^{-16}	70	14.0 [a)]
PPP-MFMR *Nanosensors #2*			
Co/Pt #1 and #2	-3.15 ×10^{-16}	90	9.2 [b)]
Co/Pt #3	-4.05 ×10^{-16}	120	7.6 [b)]
PPP-LM-MFMR *Nanosensors*			
Co/Pt #1	-2.06 ×10^{-16}	90	6.0 [b)]
Co/Pt #2	-2.12 ×10^{-16}	85	6.7 [b)]
Co/Pt #3	-1.52 ×10^{-16}	85	4.8 [b)]
HR-MFM75 ML1 *TeamNanotec*			
Co/Pt #1, #2, and #3	-1.02 ×10^{-16}	70	4.1 [a)]
MESP V2 *Bruker*			
Co/Pt #1	-3.42 ×10^{-16}	100	8.5 [a)]
Co/Pt #2 and #3	-2.88 ×10^{-16}	100	7.2 [a)]
MESP V2 *Bruker #2*			
Co/Pt #1	-1.85 ×10^{-16}	80	6.3 [b)]
Co/Pt #2	-2.45 ×10^{-16}	110	5.3 [b)]
Co/Pt #3	-3.05 ×10^{-16}	110	6.6 [b)]
MESP HM V2 *Bruke*			
Co/Pt #1 and #3	-6.45 ×10^{-16}	95	17.4 [b)]
Co/Pt #2	-6.15 ×10^{-16}	95	16.6 [b)]
MESP LM V2 *Bruker*			
Co/Pt #1	-1.25 ×10^{-16}	120	2.3 [b)]
Co/Pt #2	-1.55 ×10^{-16}	120	2.9 [b)]
Co/Pt #3	-1.05 ×10^{-16}	120	2.0 [b)]
MFM01 *TipsNano*			
Co/Pt #1, #2, and #3	-1.85 ×10^{-16}	70	7.5 [a)]
MFM_LM *TipsNano*			
Co/Pt #1 and #3	-0.8 ×10^{-16}	120	1.5 [b)]
MFM_LM *TipsNano #2*			
Co/Pt #1 and #3	-1.65 ×10^{-16}	90	4.8 [b)]
Co/Pt #2	-1.48 ×10^{-16}	90	4.3 [b)]

[a)] and [b)] calibration scans taken at 150 nm and 100 nm respectively.

It is noteworthy that even after performing several scans and changing between Co/Pt, coil, and graphene, the dipole approximation remains very similar for most of the probes, e.g.

MESP LM V2 Bruker (Table 2). This indicates low probe degradation and consistency of the TTF results.

2.4. Simulation of Hall nano-sensors and coil-based calibration schemes

To validate the experimental procedure, we simulated the calibration schemes based on the nano-sized graphene Hall sensor and of the Au coil, by applying the models described in the Experimental Section. The stray field from the MFM probe was determined by approximating the MFM probe as a point-dipole, whose parameters (z-component of the magnetic moment and mean vertical distance δ from active sensor or coil surface) were derived from the TTF characterization (Table 2).

Figure 5 shows the comparison between experimental and modelling results for the calibration scheme using the graphene Hall sensor, including the characterization of the electric behavior of the graphene Hall cross (see Figure 5(a) and Experimental section for further details). From the comparison of the experimental and numerical Hall maps for PPP-MFMR Nanosensors probe, reported in Figure 5(b) and (c), respectively, we can assume that the TTF approximation can be successfully used to reproduce the Hall sensor calibration scheme. Indeed, the match extends to all the probes tested, as it can be seen by the comparison of the experimental (i.e. Figure 5(d) and (f)) and numerical profiles of the Hall voltage signal (i.e. Figure 5(e) and (g)). It is important to point out that all the profiles shown in Figure 5(d) to (g) were taken at the same total distance from the sample's surface (i.e. 100 nm), and thus they are a proper tool to evaluate both intensity of the stray field from each probe and it's spatial decay. It is noteworthy that, in the case of the HR-MFM75 ML1 TeamNanotec probe, a distance of 150 nm was chosen, as it was the minimum distance where it was possible to image the Co/Pt sample without reversing the magnetization of the probe while scanning.

By using the Hall voltage profiles as an indication of the MFM probes field strength, we observe that for all manufacturers the “high” moment probes (e.g. MESP HM V2 Bruker, PPP-MFMR Nanosensors #2, and MFM01 TipsNano) have indeed generated higher field magnitude than the ones branded as “low” moment (e.g. MESP LM V2 Bruker, PPP-LM-MFMR Nanosensors, and MFM_LM TipsNano #2), and that in the case of Nanosensors, even the “low” moment probe (i.e. PPP-LM-MFMR Nanosensors) is stronger than the “standard” moment probe from Bruker (i.e. MESP V2 Bruker #2). Probes from TipsNano have on average the lowest strength for both “standard” and “low” moment (without knowing how the field decays for the HR-MFM75 ML1 TeamNanotec probe it is not possible to say if it is effectively the one with the lowest moment or if this is only due to the larger distance of the probe to the sensor).

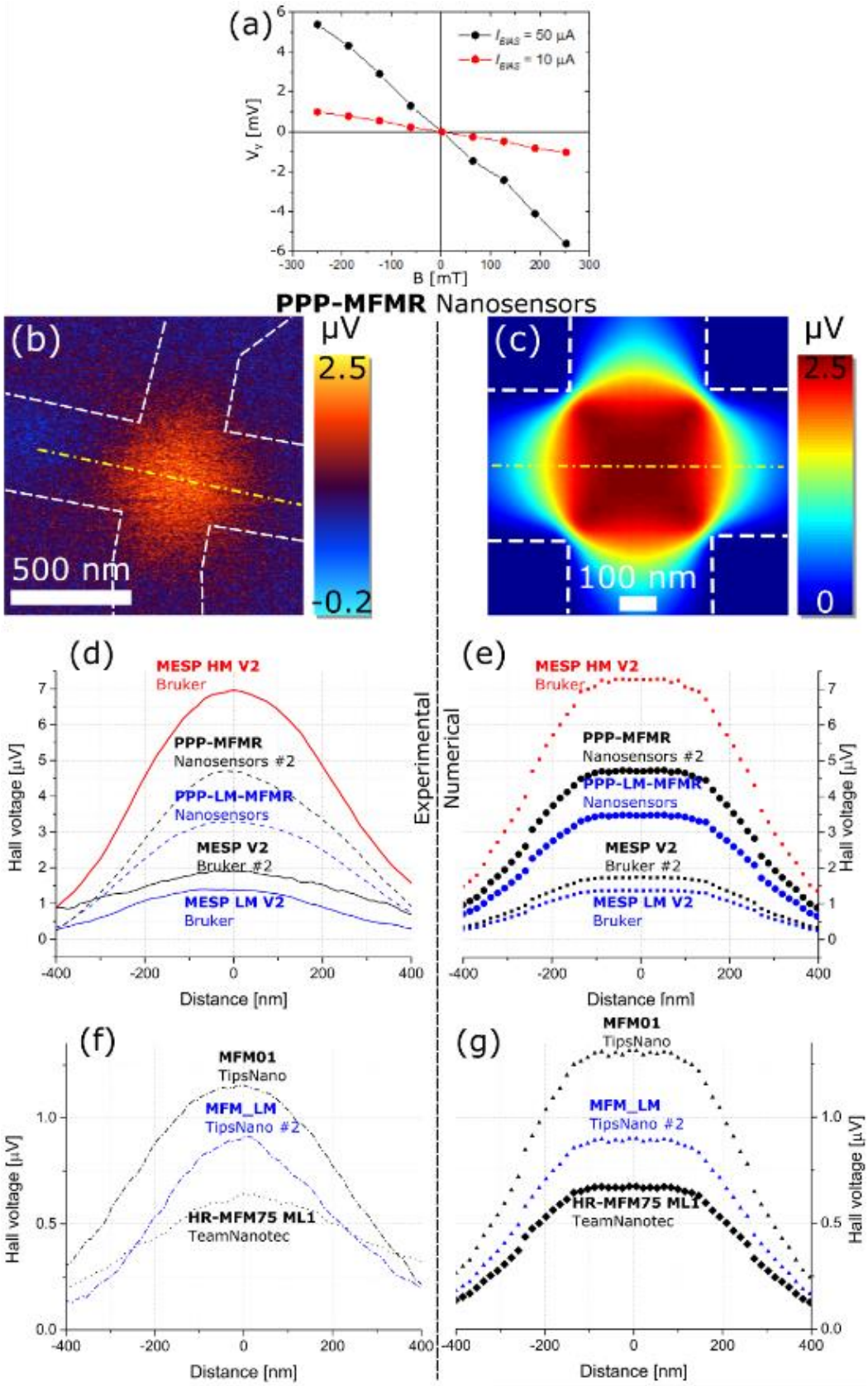

Figure 5. Hall cross response for the dipole approximations. (a) Hall voltage signal from the graphene Hall cross measured at two different DC currents, as a function of the applied magnetic field. (b) and (c) results from experimental Hall measurements and numerical simulations, respectively, for the PPP-MFMR Nanosensors. Yellow dashed lines indicate

where the experimental ((d) and (f)) and numerical ((e) and (g)) profiles for all the probes were taken. Note different voltage scales for (d-e) and (f-g).

Figure 6 shows the comparison between experimental and modelling results for the calibration scheme using the Au coil and the PPP-MFMR Nanosensors probe. As it emerges from the comparison of Figure 6(a) and (b), which report, respectively, the experimental and numerical maps of the phase shift, the point-dipole approximation from the TTF analysis does not adequately reproduce the measurement results either quantitatively or quantitatively (different shapes and range). This discrepancy can be explained by analyzing the decay of the stray field from each sample (i.e. the Co/Pt reference film and the Au coil) and its probe-interacting volume (schematized in Figure 6(c)). In the case of the Co/Pt film, the main contribution to the sample-probe magnetic coupling occurs in a small volume at the probe apex. This is justified by the fact that at greater distances from the apex there is a similar amount of upward and downward flux lines causing both attraction and repulsion interactions, and thus the contribution from the rest of the probe tends to cancel out. This is well demonstrated by Figure 6(d) and (f), which report respectively the map of the stray field from the Co/Pt film, calculated on a plane orthogonal to the film surface, and a profile taken at a distance of 200 nm (see Experimental Section for further details). Meanwhile, in the case of coils, the interaction volume adds up due to the generated stray field pattern (see simulation results in Figure 6(e) and (f)) and thus the apex is not the only part interacting. In this case, a larger volume of the probe has to be taken into account[12], effectively resulting in a different point dipole approximation than the one initially chosen from the many that can be used to approximate the TTF (see the scheme in Figure 6(c)). Hence, while the same TTF (i.e. gradient of probe's stray field at samples surface) can be fitted with many dipole approximations, the coil-probe interaction requires a very specific dipole approximation that takes into account the larger interacting volume.

To find the dipole approximation that satisfies the two constrains at the same time, and thus demonstrate that the two calibration methods are not incompatible a series of simulations of coil and dipole interactions were performed, where both the dipole magnetic moment and *z*-position were varied, with the constraint that the overall field at the coil active surface matches that obtained with the TTF approach. Figure 6(g) shows how the dipole magnetic moment has to change depending on the distance from the surface where it is located (in black) to satisfy the TTF constrain, and the maximum phase shift resulting from using that dipole when simulating the coil-probe interaction. It is possible to see that there is an optimal equivalent dipole approximation ($m_{eq} \sim -1.09 \times 10^{-13}$ Am^2 and $\delta_{eq} = 1435$ nm [i.e. 1285 nm from the probe's apex]) that enables us to obtain a good agreement between the TTF and the requirement imposed by the coil calibration scheme (i.e. the total phase shift matching that of Figure 6(a)). This is further corroborated by the calculated maps of the phase shift shown in Figure 6(h) to (j), where for the optimal dipole moment value and position the numerical map matches not only the amplitude, but also the shape of the experimental results (i.e. Figure 6(a)). It is thus demonstrated that the two calibration methods are compatible and lead to a coherent description of the probe-sample interaction.

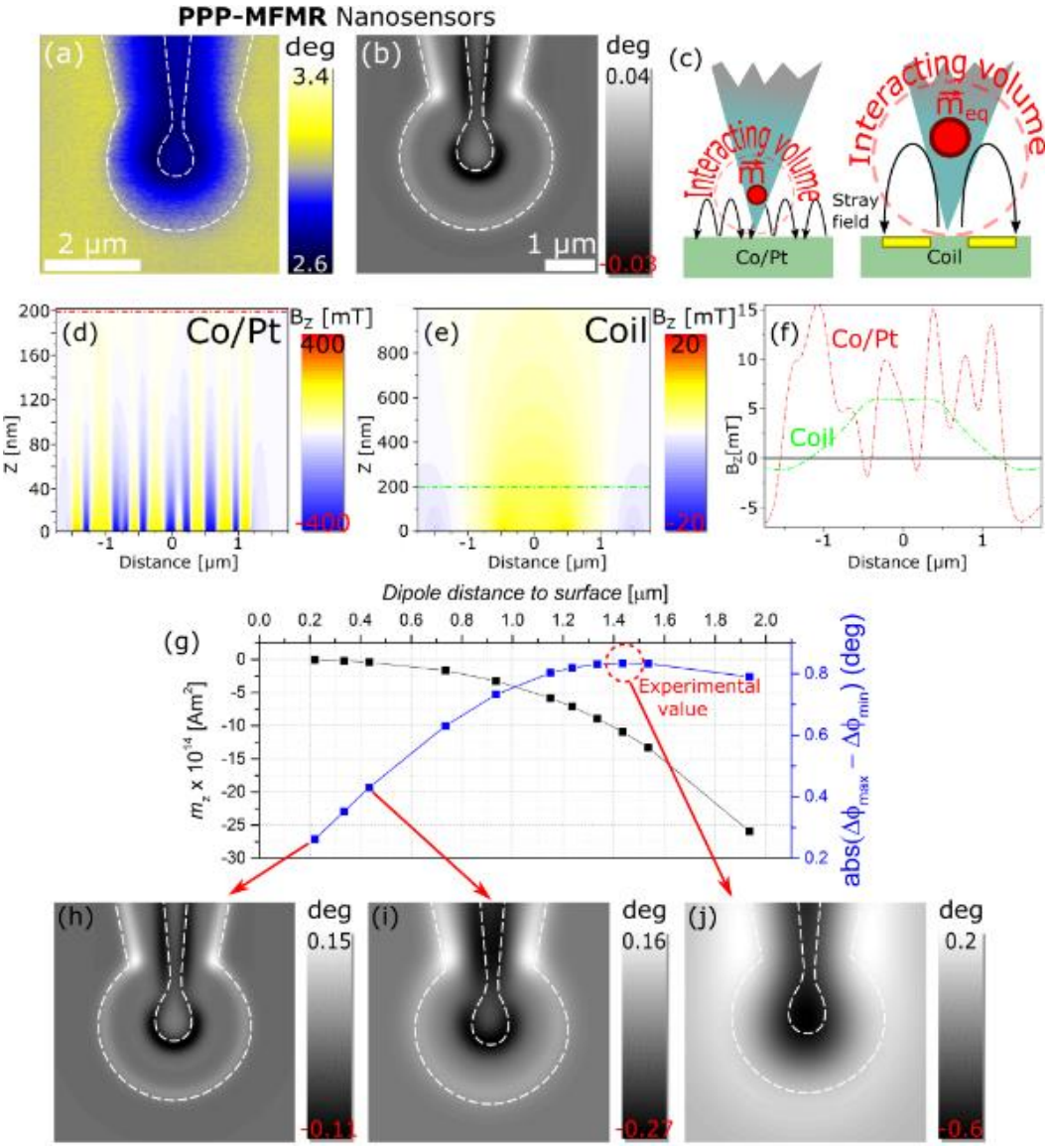

Figure 6. MFM probe calibration using Au coil. Comparison of experimental (a) and numerical (b) phase shift images for the PPP-MFMR Nanosensors probe. The numerical map was obtained by considering the dipole parameters provided by the TTF approximation. (c) Schematics depicting different interacting volumes between probe and sample depending on sample's stray field for Co/Pt (left) and coil (right). (d) and (e) Calculated maps of the z-component of the stray field above the Co/Pt film (left) and coil (right) when a 10 mA current is injected. Dashed lines indicate where the profiles shown in (f) were taken. (g) Variation of equivalent dipole magnetic moment z-component (black curve) as a function of the distance of the dipole from the coil active surface. The moment amplitudes are estimated as the ones able to match the TTF approximation in terms of stray field at the sample surface. The blue curve describes the maximum variation of the phase shift, calculated for the corresponding equivalent dipole. Red circle indicates the phase shift value that agrees with the experimental result shown in (a). (h) to (j): numerical maps of the phase shift for different positions and magnetic moment amplitude of the equivalent dipole.

3. Conclusion

We have demonstrated the versatility and reliability of the TTF approach to calibrate magnetic probes and thus attain quantitative MFM imaging. This was achieved by using the calibration based in the TTF approach to approximate the probe by a magnetic dipole and then predicting the sample-probe interaction present in other two calibration techniques, the one based on the use of micron-size coils and the one that uses nano-sized graphene Hall sensors. In the case of Hall sensors, all the possible dipole approximations of the TTF calibration are able to reproduce numerically the experimental results from the Hall cross. However, in the case of coils, the larger probe-sample interacting volume act as an additional constrain resulting in a single dipole being able approximate the TTF and reproduce the coil-probe interaction. Thus demonstrating that the TTF and the other two calibration methods produce a coherent calibration for each probe.

Additionally, the results reported include the magnetic dipole approximation for a range of commercial probes, and show an agreement between nominally "high/low" "moment" probes and large/small amplitude of the approximating magnetic dipole.

We conclude that the TTF approach is a robust method to calibrate MFM probes and it can be used to approximate probes with multipole expansions, and that by taking into account the pattern of the sample's stray field (and thus the interacting volume), it is possible to reproduce the sample-probe interaction for a wide range of magnetic samples.

4. Experimental Section

4.1. SPM imaging

The AFM imaging was performed using NT-MDT Ntegra-AURA scanning probe microscopy system, adapting the scanning modes to match those described here and shown in Figure 1. In combination with the AFM system, an auxiliary power supply was used to power the coil and the graphene Hall cross: Keithley 2400 SourceMeter. A lock-in amplifier (model SR830) was used to measure the Hall voltage.

The calibration protocol applied for each probe (shown in Figure 3 for the PPP-MFMR Nanosensors probe) was as follows[16]:

1 The cantilever chip was mounted in the SPM system and the laser and photodiode system were aligned.

2 A frequency spectrum was taken to find the resonance frequency (see further details in the Supporting Information) which is then used to oscillate the probe close to its resonance frequency (i.e. typically 5% off resonance). The spring constant and quality factor were measured using the standard built-in features of the scanning probe microscope (i.e. the spring constant was measured using thermal tuning).

3 An out-of-plane electromagnet was used to sweep the magnetic field while monitoring the deflection, amplitude and phase shift of the probe (see further details in the Supporting Information) to determine the coercive field of each probe in order to avoid artefacts while imaging (i.e. by knowing how much magnetization changes with field).

4 In order to guarantee that the probes were in saturated state prior to imaging, a permanent magnet was used to fully saturate the probe's magnetization.

5 The probes were then engaged (i.e. "landed" or approached) into the surface of Co/Pt and a ramp, varying the distance to the sample's surface, was performed to measure the oscillation amplitude and the setpoint distance to the sample surface.

6 Standard 2-pass MFM was used to image an area of 10 μm by 10 μm at 512 by 512 pixels, as shown in Figure 3(a). It was important at this point, in some cases, to readjust the setpoint to make sure that the topography (i.e. Figure 3(a)(1)) didn't show an intense signal from the stray field (i.e. resembling features of the magnetization shown Figure 3(a)(2)). The ramp taken in step 5 was then used to: calculate the lift height needed to obtain the total distance to sample desired during the second pass; and to adjust the oscillation amplitude so that during the second pass the phase images are artefact free and the probe is in the free

oscillation regime. Several images were acquired for each probe, in order to identify artefacts, or to reduce noise by averaging the signal in post-processing.

7 The Co/Pt sample was replaced by the graphene Hall cross and a DC current of 50 µA was applied.

8 After engaging the surface, a ramp was performed to obtain the same oscillation amplitude and distance as with the Co/Pt sample.

9 PM-mSG-KPFM was used to image the graphene (as shown in Figure 3(b)), registering both the in-phase and out-of-phase signals from the Hall cross with the lock-in locked at the probe's excitation frequency. The scan speed was adjusted so the time per pixel was at least three times the time constant of the lock-in (i.e. 3 ms in this case and 2.5 µm scan size to maintain the same pixel size as with Co/Pt). To guarantee that the best electrical compensation parameters are used, trace and retrace signals were compared and the parameters were adjusted until both signals matched each other (surface potential shown in Figure 3(b)(2)). When the electrical compensation is optimized the Hall signal takes the shape of a circular spot at the center of the cross, as previously reported in Ref[18][17][10] and shown in Figure 3(b)(3). If the electrostatic field is not fully compensated, dark and bright lobes will appear at the edges/corners of the cross, due to capacitive coupling between the probe and the device[17].

10 The graphene was then replaced by the Co/Pt and steps 5 and 6 were repeated to obtain a second calibration after imaging the Hall cross. Another measurement of the spring constant and quality factor was performed to identify possible damage to the probes.

11 The Co/Pt was then replaced by the embedded coil and after engaging the surface a ramp was performed to adjust the setpoint and oscillation amplitude to match those used when imaging the Co/Pt and the graphene Hall cross.

12 PM-MFM-KPFM imaging was performed while passing a current of 10 mA through the coil. As with the graphene, it was important to check that the electrostatic

compensation was working properly by looking at the surface potential (i.e. Figure 3(d)(2)) and comparing the trace and retrace signals. Scans with positive and negative currents passing through the coil were performed to guarantee artefact-free imaging (only one current direction shown in Figure 3(d)(3)).

13 Finally, Co/Pt imaging was performed to obtain a third calibration. The spring constant and quality factor were also measured to check if the probe properties changed during the whole process.

4.2. Coil fabrication

The embedded coils were fabricated on a silicon wafer with 300 nm oxide using electron beam lithography and conventional lift-off processes. The coils consist of a 50 nm gold layer that was deposited by electron beam evaporation. A 5 nm layer of titanium was used as an adhesion agent. In a second step an additional 50 nm thick gold layer was deposited on the contact area. To embed the coils 188 nm of thermal silicon oxide was deposited by plasma-enhanced chemical vapor deposition on top of the structures. This material thickness was needed to avoid holes in the capturing layer. However, for MFM, the sensor-sample distance should be small, so the oxide was thinned using chemical-mechanical polishing. The final oxide thickness over the coil is (50 ± 20) nm, while the contact pads are oxide free.

4.3. Hall sensor fabrication

Hall sensors composed of 200 nm-wide single layer epitaxial graphene on 6H-SiC(0001) were fabricated using the procedures reported in Ref[19]. Magnetotransport measurements were performed on the device, ramping magnetic field and measuring Hall voltage while applying a constant current of 10 μA, resulting in a carrier density, $n_e = -1.54 \times 10^{16}$ m^{-2}, and a carrier mobility, $\mu e = 0.0085$ $m^2V^{-1}s^{-1}$, at room temperature and in ambient air.

4.4. Co/Pt multilayer sample fabrication

The Co/Pt reference sample was prepared by magnetron sputtering with the following layer architecture Pt(2nm)/[(Co(0.4nm)/Pt(0.9nm)]$_{100}$/Pt(5nm)/Ta(5nm)/SiOx/Si(100) [20]. The total thickness of the magnetic layer is 130 nm and owing to the interface anisotropy of the thin Co layers the film develops magnetic anisotropy perpendicular to the surface. In zero field the magnetization of the multilayer collapses into a band domain pattern with average domain width of 170 nm. Global magnetization measurements determine the saturation magnetization to be M_s = 500 kA/m (error ± 30 kA/m) and confirm the perpendicular magnetization through a ratio $Q_u = K_u/K_d = 2.5$ (K_u = 0.4 MJ/m^3 is the perpendicular anisotropy constant, $K_d = 0.5\ \mu_0 M_s^2$ = 0.16 MJ/m^3 is the magnetostatic energy density). The Bloch type domain transition has a width of about 16 nm. The band domain pattern of the reference sample develops homogeneously across the whole sample, thus arbitrary sample positions have been chosen.

4.5. Numerical modeling

The map and the spatial profiles of the simulated Hall voltage signal reported in Figure 5 were calculated by means of a custom-made two-dimensional finite element code[21,22]. This allowed us to determine the spatial distribution of the electric potential ϕ within the n-doped graphene Hall cross under the effect of the localized stray field produced by an MFM probe. By assuming diffusive transport regime for the electron transport, we solved the following equation:

$$\nabla \cdot [\tilde{\sigma}(\mathbf{r})\nabla\phi(\mathbf{r})] = 0\ . \tag{1}$$

The conductivity tensor $\tilde{\sigma}(\mathbf{r})$ in (1) is expressed as

$$\tilde{\sigma}(\mathbf{r}) = \frac{e\mu_e n_e}{1+[\mu_e B_{probe}(\mathbf{r})]^2}\begin{bmatrix} 1 & \mu_e B_{probe}(\mathbf{r}) \\ -\mu_e B_{probe}(\mathbf{r}) & 1 \end{bmatrix}, \tag{2}$$

where e is the electron charge, n_e is the electron density and μ_e is the electron mobility.

The component of the probe magnetic field perpendicular to the sensor surface (B_{probe}) was determined by approximating the MFM probe as a point-dipole, whose parameters (z-component of magnetic moment and mean vertical distance δ from graphene surface) were

derived from the TTF characterization (Table 2). A parameter variation in the range of ±5% was introduced to obtain the best fit with experimental results. The effect of probe oscillation (amplitude $\Delta\delta$) was modelled by subtracting the Hall voltage values obtained at the maximum distance between probe and graphene surface (δ+$\Delta\delta$) from the ones corresponding to minimum distance (δ-$\Delta\delta$).

In the simulations of coil calibration scheme (see Figure (6)), the phase shift of the MFM probe vibration due to the interaction with the coil magnetic stray field $\mathbf{B}_{coil}$ was approximated as

$$\Delta\varphi = -\frac{180}{\pi}\frac{Q}{k}\left[m_x\frac{\partial^2 B_{coil,x}(\mathbf{r})}{\partial z^2} + m_y\frac{\partial^2 B_{coil,y}(\mathbf{r})}{\partial z^2} + m_z\frac{\partial^2 B_{coil,z}(\mathbf{r})}{\partial z^2}\right], \quad (3)$$

where Q is the cantilever quality factor and k is the cantilever spring constant[11,12]. $\mathbf{B}_{coil}$ in (3) and in Figure 5(e) was calculated with the Biot-Savart law, after the derivation of the spatial distribution of the current density vector within the coil volume, by numerically solving current field equation under static conditions.

In (3) the MFM probe was modeled again as a point-dipole, with $m_x = m_y = 0$. As explained in the Results Section, when considering the parameters from the TTF characterization, a strong discrepancy was found between the calculated and experimental maps of $\Delta\varphi$, in terms of both spatial distribution and amplitude of the signal. The reason is that the value of the distance between the point-dipole and the coil surface predicted by the TTF analysis is so low to lead to an underestimation of the effective probe volume interested by the coil stray field (Figure 5(c)). To properly reproduce the spatial decay of the coil-probe magnetic interaction, we searched for an equivalent point-dipole representation, gradually increasing its distance δ from the coil active surface. The derivation of the corresponding z-component of the magnetic moment was performed to obtain approximately the same probe stray field at the coil surface, namely

$$m_{eq,z} = m_{TTF,z}\left(\frac{\delta_{eq}}{\delta_{TTF}}\right)^3. \quad (4)$$

Finally, the map of the stray field generated by the Co/Pt film (Figure 5(d)) was calculated, after discretising the magnetic sample into *N* hexahedra, by solving the following equation:

$$\mathbf{B}(\mathbf{r}) = \frac{\mu_0}{4\pi}\sum_{i=1}^{N}\int_{\partial\Omega_i}\mathbf{M}(\mathbf{r}_i)\cdot\mathbf{u}_i\frac{(\mathbf{r}-\mathbf{r}_i)}{\|\mathbf{r}-\mathbf{r}_i\|^3}ds, \quad (5)$$

where $\partial\Omega_i$ is the surface of the *i*-th hexahedron having normal unit vector $\mathbf{u}_i$ and barycentre with vector position $\mathbf{r}_i$[23] The imposed spatial distribution of magnetization vector **M** was reconstructed from MFM images of the sample, taken as close as possible to the surface.

4.6. TTF calculation

The TTF approach is based on the exact description of the MFM phase shift signal as a 2-dimensional convolution of the effective surface charges, σ, of the sample with the probe's 2-dimensional stray field derivative profile at the same surface $\frac{\partial H_z^{probe}}{\partial z}$. It is mathematically derived from the magnetostatic sample-probe interaction as a 3-dimensional volume integration of the sample's stray field and an arbitrary and rigid magnetization distribution across the whole volume of the magnetically coated tip[13], under the sole condition that the measurement is performed in a plane parallel to the sufficiently flat and extended sample surface. In the discrete form of measured MFM data this reads:

$$\Delta\Phi(x_i, y_j, z_0) = \frac{Q}{k}\frac{180}{\pi}\cdot\frac{\partial F_z}{\partial z}(x_i, y_j, z_0)$$

$$=\frac{Q}{k}\frac{180}{\pi}\cdot\Delta x\cdot\Delta y\cdot\mu_0\cdot\sigma\left(x_i - x'_i, y_j - y'_j, 0\right)\cdot\frac{\partial H_z^{probe}}{\partial z}\left(x'_i, y'_j, d = -z_0\right) \quad (6)$$

which is a simple matrix multiplication in Fourier space:

$$\Delta\Phi(kx_i, ky_j, z_0) = \frac{Q}{k}\frac{180}{\pi}\cdot\mu_0\cdot\Delta x\cdot\Delta y\cdot\sigma^*(kx_i, ky_j, 0)\cdot TTF(kx_i, ky_j, d = -z_0) \quad (7)$$

Here, Δx and Δy are the pixel size during imaging, and the probe's stray field derivative $\frac{\partial H_z^{probe}}{\partial z}$,named TTF, is taken at the distance z_0 below the apex of the tip.

The phase shift data is converted into modified force gradient data by multiplying with $\left[\frac{Q}{k}\frac{180}{\pi}\cdot\mu_0\cdot\Delta x\cdot\Delta y\right]^{-1}$. This leads to a convenient matrix in units A^2/m^3, which is however different from the true force gradient by a factor $[\mu_0\cdot\Delta x\cdot\Delta y]^{-1}$. In Gwyddion, this modified force gradient is named the Pixel area MFM force gradient (i.e. steps 3 and 4 in Section 4.7. Gwyddion Post-processing).

The effective surface charge of the imaged band domain pattern can be derived from the measured phase shift image after an image plane correction by identifying regions with $\Delta\Phi>0$ as positive domains with $\vec{m}=(0,0,M_s)$ and regions with $\Delta\Phi<0$ with $\vec{m}=(0,0,-M_s)$ (i.e. step 5 in section 4.7. Gwyddion Post-processing). The magnetization pattern leads to a surface charge pattern $\sigma=\vec{m}\cdot\vec{n}=\pm M_s$ on the upper surface of the reference sample ($\vec{n}$ is the surface normal), and to $\mp M_s$. at the corresponding lower sample surface, which is located *t* = 130 nm below (i.e. step 6 in section 4.7. Gwyddion Post-processing). The effective surface charge σ^*, i.e. the projection of all magnetic charges onto the upper surface of the sample is given by

$$\sigma^*(kx,ky)=M_s(1-e^{-k\cdot t})\cdot\sigma(kx,ky) \tag{8}$$

in Fourier space. $k=\sqrt{kx^2+ky^2}$ is the modulus of the spatial frequency vector (*kx*,*ky*). The smooth magnetization transition of the domain walls is considered by convolving the effective surface charge pattern with an operator of the form[24][20] $f(x,y)=1/cosh\left(\frac{\pi\sqrt{x^2+y^2}}{\delta_w}\right)$, with the domain wall width δ_w.

The TTF is obtained by deconvolving the modified force gradient matrix with $\sigma^*(kx_i,\ ky_i)$ as the kernel. Both input matrices were multiplied by a Welch windowing function to reduce artefacts from image boundaries[14]. For de-noising, a Wiener filter with an adapted regularization parameter is applied. This is appropriate for Gaussian type noise with zero expectation value present in MFM data. In SigMath[25], the Wiener filter is implemented from

the Clarity Deconvolution Library[26], in Gwyddion, the optimum regularization parameter is chosen by means of the L-curve criterion[2] (i.e. step 7 in section 4.7. Gwyddion Post-processing).

4.7. Gwyddion post-processing

This step-by-step guide describes procedurally how the TTF was calculated from the standard 2-pass MFM measurements using Gwyddion version 2.53.20190809. For further details, see the online documentation[27].

1 The phase change image was loaded into Gwyddion.

2 "Align rows" was used to correct artefacts due to changes between lines. In some cases, several scans were averaged together loading the images into Gwyddion and using Data Process>Multidata>Arithmetic

3 The data was leveled around zero using Data Process>Level>Zero Mean Value.

4 The phase change image was then converted into force gradient using Data Process>SPM modes>Magnetic>Recalculate to force gradient and inputting the probe's spring constant and Q factor. It was selected "Pixel area MFM force gradient" as "Result type".

5 A mask was used to mark the different domains prior to simulate sample's stray field using Data Process>Grains>Mark by Otsu's.

6 The masked image was used to simulate the sample's stray field using Data Process>SPM modes>Magnetic>Perpendicular Media Stray Field and inputting the sample's parameter, which in this case are: output plane height 0 nm; film thickness 130 nm; magnetic charge 510 kA/m. M_{eff} was selected as desired output.

7 To obtain the TTF (i.e. probe's stray field gradient at sample's surface), the pixel area force gradient image with the mask and the M_{eff} image, calculated in step 6, were deconvolved using Data Process>Multidata>Deconvolve. The deconvolution kernel was the

image M_{eff} and the windowing type "Welch". "Update L-curve" function was used to select the position of the maximum of the L-curve which provides the best deconvolution. (Note: "Normalize as integral" was deselected).

Supporting Information
Supporting Information is available from the Wiley Online Library or from the author.

Acknowledgements
The authors acknowledge the financial support from the European Metrology Programme for Innovation and Research (Grant No. 15SIB06), NanoMag. Manuela Gerken gratefully acknowledges the support of the Braunschweig International Graduate School of Metrology B-IGSM and the DFG Research Training Group 1952 Metrology for Complex Nanosystems. We acknowledge C. Krien for preparing the Co/Pt multilayer reference sample.

Received: ((will be filled in by the editorial staff))
Revised: ((will be filled in by the editorial staff))
Published online: ((will be filled in by the editorial staff))

References

[1] O. Kazakova, R. Puttock, C. Barton, H. Corte-León, M. Jaafar, V. Neu, A. Asenjo, *J. Appl. Phys.* **2019**, *125*, 060901.

[2] X. K. Hu, G. Dai, S. Sievers, V. Neu, H. W. Schumacher, *CPEM 2018 - Conf. Precis. Electromagn. Meas.* **2018**, 5.

[3] S. McVitie, R. P. Ferrier, J. Scott, G. S. White, A. Gallagher, *J. Appl. Phys.* **2001**, *89*, 3656.

[4] S. Signoretti, C. Beeli, S.-H. Liou, *J. Magn. Magn. Mater.* **2004**, *272–276*, 2167.

[5] H. Corte-León, L. A. Rodríguez, M. Pancaldi, C. Gatel, D. Cox, E. Snoeck, V. Antonov, P. Vavassori, O. Kazakova, *Nanoscale* **2019**, *11*, 4478.

[6] M. Jaafar, A. Asenjo, M. Vázquez, *IEEE Trans. Nanotechnol.* **2008**, *7*, 245.

[7] H. Corte-León, A. F. Scarioni, R. Mansell, P. Krzysteczko, D. Cox, D. McGrouther, S. McVitie, R. Cowburn, H. W. Schumacher, V. Antonov, O. Kazakova, *AIP Adv.* **2017**, *7*, 056808.

[8] M. Seifert, I. Knittel, U. Hartmann, L. Schultz, V. Neu, *J. Phys. D. Appl. Phys.* **2012**, *45*, 175001.

[9] F. Wolny, T. Mühl, U. Weissker, K. Lipert, J. Schumann, A. Leonhardt, B. Büchner, *Nanotechnology* **2010**, *21*, 435501.

[10] V. Panchal, H. Corte-León, B. Gribkov, L. A. Rodriguez, E. Snoeck, A. Manzin, E. Simonetto, S. Vock, V. Neu, O. Kazakova, *Sci. Rep.* **2017**, *7*, 7224.

[11] T. Kebe, A. Carl, *J. Appl. Phys.* **2004**, *95*, 775.

[12] J. Lohau, S. Kirsch, A. Carl, G. Dumpich, E. F. Wassermann, *J. Appl. Phys.* **1999**, *86*, 3410.

[13] H. J. Hug, B. Stiefel, P. J. a. van Schendel, a. Moser, R. Hofer, S. Martin, H.-J. Güntherodt, S. Porthun, L. Abelmann, J. C. Lodder, G. Bochi, R. C. O'Handley, *J. Appl. Phys.* **1998**, *83*, 5609.

[14] D. Nečas, P. Klapetek, V. Neu, M. Havlíček, R. Puttock, O. Kazakova, X. Hu, L. Zajíčková, *Sci. Rep.* **2019**, *9*, 1.

[15] D. Nečas, P. Klapetek, *Open Phys.* **2012**, *10*, 181.

[16] *NTI/1_19_0193. Nanomanufacturing – Key Control Charact. – Part 9-1 Nanoscale stray Magn. F. Meas. Magn. force Microsc.* **2019**.

[17] R. K. Rajkumar, A. Asenjo, V. Panchal, A. Manzin, Ó. Iglesias-Freire, O. Kazakova, in *J. Appl. Phys.*, **2014**, pp. 2–7.

[18] V. Panchal, O. Iglesias-Freire, A. Lartsev, R. Yakimova, A. Asenjo, O. Kazakova, *IEEE Trans. Magn.* **2013**, *49*, 3520.

[19] L. O. Nyakiti, V. D. Wheeler, N. Y. Garces, R. L. Myers-Ward, C. R. Eddy, D. K. Gaskill, *MRS Bull.* **2012**, *37*, 1149.

[20] S. Vock, C. Hengst, M. Wolf, K. Tschulik, M. Uhlemann, Z. Sasvári, D. Makarov, O. G. Schmidt, L. Schultz, V. Neu, *Appl. Phys. Lett.* **2014**, *105*, 172409.

[21] R. K. Rajkumar, A. Manzin, D. C. Cox, S. R. P. Silva, A. Tzalenchuk, O. Kazakova,

IEEE Trans. Magn. **2013**, *49*, 3445.

[22] V. Nabaei, R. K. Rajkumar, A. Manzin, O. Kazakova, A. Tzalenchuk, *J. Appl. Phys.* **2013**, *113*, 064504.

[23] A. Manzin, O. Bottauscio, *J. Appl. Phys.* **2012**, *111*, 07D125.

[24] S. Vock, Z. Sasvari, C. Bran, F. Rhein, U. Wolff, N. S. Kiselev, A. N. Bogdanov, L. Schultz, O. Hellwig, V. Neu, *IEEE Trans. Magn.* **2011**, *47*, 2352.

[25] *SigMath = http//sig.math.tu-dresden.de/index.shtml* **n.d.**

[26] *Clarity = Clarity Deconvolution Libr. [Online]. Available http//cismm.web.unc.edu/resources/software-manuals/clarity-deconvolution-library* **n.d.**

[27] "Gwyddion documentation: Magnetic force microscopy. Chapter 4. Data Processing and Analysis.," can be found under http://gwyddion.net/documentation/user-guide-en/mfm.html, **n.d.**

Magnetic force microscopy, which enables imaging magnetic fields with nanoscale resolution, and is a critical tool for developing new consumer electronics, has been an uncalibrated technique for many years. Here, calibration approaches based on reference samples, graphene Hall sensors, and micron-sized coils are compared and validated using numerical modelling to link the experimental results and to demonstrate that calibrated MFM became a reality. Furthermore, the calibration method based on reference samples is demonstrated here step-by-step with the aid of the open source software Gwyddion, thus allowing other researchers, to obtain quantitative measurements without prior knowledge of MFM calibration methods.

Keyword MFM, calibration, magnetic probes, Hall nano-sensors, nanoscale,

Héctor Corte-León, Volker Neu, Alessandra Manzin, Craig Barton, Yuanjun Tang, Manuela Gerken, Petr Klapetek, Hans Werner Schumacher and Olga Kazakova.*

Comparison and validation of different magnetic force microscopy calibration schemes